Seasonal Variations of the Atmospheric Muon Rate at KM3NeT

Hernandez Sanz, Maria

Seasonal Variations of the Atmospheric Muon Rate at KM3NeT

THESIS

submitted in partial fulfillment of the
requirements for the degree of

BACHELOR OF SCIENCE
in
PHYSICS

Author :	María Hernández Sanz
Student ID :	2166135
Supervisor :	Dorothea Samtleben
Second corrector :	Tjerk Oosterkamp

Leiden, The Netherlands, July 5, 2022

Seasonal Variations of the Atmospheric Muon Rate at KM3NeT

María Hernández Sanz

Huygens-Kamerlingh Onnes Laboratory, Leiden University
P.O. Box 9500, 2300 RA Leiden, The Netherlands

July 5, 2022

Abstract

In hopes of understanding the universe we inhabit, scientists search for signals from the universe that could give as clues about its nature. When these signals are composed of particles, they are given the name of "cosmic rays". Once cosmic rays have reached our atmosphere, they interact with molecules there, creating pions and kaons that decay into muons and neutrinos. Studying these, we can deepen our knowledge and understanding of the universe. It is in the interest of this that this thesis explores the effect of seasonal changes in temperature on the rate of atmospheric muons that reaches the ARCA site of KM3NeT, a neutrino telescope being built in the Mediterranean sea. Exploiting their depth dependence we were able to establish a new method to quantify a muon rate, allowing the investigation of different energy ranges through the filtering of certain coincidences. After fitting these curves to an exponential decay, the fit parameters were extracted and compared to the temperatures in different pressure levels of the atmosphere. This showed a weak negative correlation for the normalization factor and a moderate positive correlation for the slope. For lower energies, the relationship between the slope and temperature was proportional by a factor $\alpha_T = 0.0029 \pm 0.00012$. For higher energies, this proportionality was given by $\alpha_T = 0.0051 \pm 0.00034$. Due to the weak correlation exhibited, no constant of proportionality was found for the normalization factor.

Contents

Version of July 5, 2022– Created July 5, 2022 - 14:12

Version of July 5, 2022– Created July 5, 2022 - 14:12

Chapter 1

Introduction

"Our knowledge springs from two fundamental sources of the mind; the first is the capacity of receiving representations, the second is the power of knowing an object through these representations."

Immanuel Kant

This is how philosopher Immanuel Kant explains, in his *Critique of Pure Reason*, the human ability to understand the world outside of us. We *know* thanks to our reception of representations and the potential of interpretation. Physicists defy these "fundamental sources of the mind" by creating instruments that improve our capacities to receive information otherwise hidden and by finding ways to translate it into parameters we can understand and analyze. A good example of such instruments are telescopes.

When thinking about telescopes, it is common to imagine large structures looking towards the universe, recording photon or radio signals and amplifying them for our senses. However, this is not the only way to do astronomy. A relatively new and exciting mode of studying the universe emerged this century, namely: Neutrino Astronomy. Neutrino telescopes make use of the amount of detected particles from astrophysical sources in order to explain our universe in different terms. The particles observed however, are not like any other particles.

Neutrinos were only first postulated in 1930 by Wolfgang Pauli who categorized them as a "desperate remedy" to the energy distribution of electrons after beta decay [1]. It was only 26 years later that the existence of this particle was quantified.

The reason behind such reluctance to the accept neutrinos is the fact that they are the most elusive particles in the universe. Not only do they

have nearly no mass but they are also able to travel extremely long distances without interacting with any other particles or electromagnetic fields. Neutrinos may be affected by the weak force yet due to the minuscule range this force acts in, they are able to traverse massive objects as if they were empty. This makes neutrinos extremely informative of the sources they are generated in as no information is lost on their way to reception.

Accordingly, neutrino telescopes are built deep in the Earth, filtering any other particles that are bound to interact along their journey. Such is the case of the KM3NeT telescope, whose data will be used in this thesis, and that is currently being built in the depths of the Mediterranean sea. KM3NeT makes use of the Cherenkov radiation produced when neutrinos travel through water to study their characteristics. However, being built in nature, there is a large amount of background noise reaching the detector that must be filtered out if we want to focus solely on neutrinos. This thesis will study an important source of noise, namely atmospheric muons.

Every day, we are being bathed in showers of high energy rays that reach our atmosphere and interact with other particles there, producing showers of muons and neutrinos. These energetic muons reach the sea and produce Cherenkov light, triggering an event in KM3NeT's detector.

The goal of this thesis is to investigate the relation between the amount of muons created in the atmosphere and the temperature of the latter throughout the seasons. By exploiting the depth dependence of the muons, a stable method will be established and a reliable rate will be quantified. While similar studies have been carried out by KM3NeT and other neutrino telescopes, the rate was established through different methods and the enegy spectrum was different to that of KM3NeT.

Understanding how the muon rate varies with seasons will allow for a deeper grasp of the properties of muons and might provide explanations for slight deviations in the expected neutrino flux pattern.

Chapter 2

Theoretical Background

2.1 Cosmic Rays

Our universe is composed of numerous structures and astrophysical objects. Supernovas, binary stars, black holes collisions are dynamic events that send information loaded signals to Earth. When these signals use particles as a medium, they are given the name of "cosmic rays".

Cosmic rays were first discovered by Victor Hess in 1912 while studying radiation from the Earth's crust. The experiment designed for this quest consisted of carrying an ionization chamber in a hot air balloon to 5300 metres above the Earth's surface. According to his hypothesis, the level of ionization should have been lower the farther from the crust. Contrarily, he noticed that the higher in the atmosphere he went, the higher the ionization rate. In fact, he measured 3 times that of the ionization at sea level [2]. This suggested an increase in particles available for interaction. Having carried out his experiment during a solar eclipse, he was able to discard the most logical hypothesis of particles coming from the sun [3], resulting in the concept of cosmic rays and a whole new world of particles that were about to be discovered [2].

2.2 Atmospheric muons

Once cosmic rays have reached our atmosphere, they interact with atmospheric molecules, producing the so called air showers. We distinguish two types of air showers depending on the particle that gives rise to it. The first type takes place when a photon, electron or positron causes the shower while the second type begins with a proton or a heavier nucleus [3].

In this investigation, the main focus will be the second type.

Figure 2.1 shows the air shower's potential developments. Some of the possible resulting particles are pions and kaons. Pions are unstable particles governed by the weak interaction force. In their decay, they produce muons as well as neutrinos. The formulas for pion decays are as follows, depending on their charge:

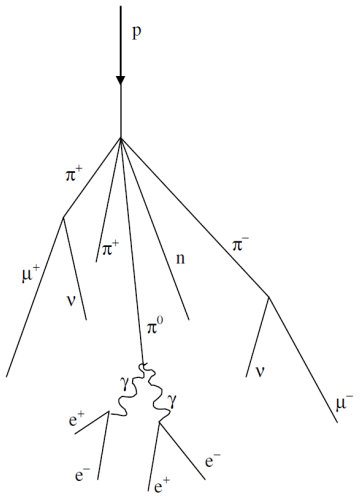

Figure 2.1: *Proton reaching the atmosphere, producing air showers of different particles.[4]*

$$\pi^+ \rightarrow \mu^+ + \upsilon_\mu \tag{2.1}$$

$$\pi^- \rightarrow \mu^- + \bar{\upsilon}_\mu \tag{2.2}$$

This type of decay will occur with a 99.99% probability.

On the other hand, kaons might also decay into neutrinos and muon neutrinos yet with a lower probability of 63.56%. The equations for such interaction are:

$$K^+ \rightarrow \mu^+ + \upsilon_\mu \tag{2.3}$$

$$K^- \rightarrow \mu^- + \bar{\upsilon}_\mu \tag{2.4}$$

As stated in the introduction, it is highly unlikely for neutrinos to interact with other particles, producing an observable quantity and thus contributing to the noise in our detectors. Therefore, we will focus on the muons created.

Like pions and kaons, muons are also unstable with a lifetime of [5]

$$\tau = 2.19 \pm 0.01 \mu s \tag{2.5}$$

However, given the theory of special relativity and the fact that they travel at speeds extremely close to that of light, they are able to reach the sea and hence the detectors without decaying.

Suppose a muon is produced at 6500 meters from the surface of the Earth, 10 000 m away from KM3NeT's detectors. If this muon was travelling at a speed of 0.998c[†], the maximum distance this muon would be able to reach in 2.19 µs according to newtonian mechanics would be:

$$d = v\tau = 0.998 \times 3 \times 10^8 \times 2.2 \times 10^{-6} = 658.68\,\text{m} \tag{2.6}$$

Yet given Lorentz' Contraction, in the muon frame the lifetime would be

$$\tau = \frac{\tau_0}{\sqrt{1 - \frac{v^2}{c^2}}} = 34.8\,\mu\text{s} \tag{2.7}$$

The maximum distance travelled then becomes:

$$d = v\tau = 0.998 \times 3 \times 10^8 \times 34.8 \times 10^{-6} = 10\,400\,\text{m} \tag{2.8}$$

Therefore, muons are able to travel long distances from the atmosphere within their lifetime.

However, the longer they travel, the more muons that will be subject to decay. Mathematically, the relationship between the intensity of the muons, power over area, and the geometric distance $r = \sqrt{x^2 + y^2 + z^2}$ is theorized to be:

$$I(r) = I_0 e^{-\frac{r}{c\tau}} \tag{2.9}$$

where τ is the lifetime and c is the speed of light[3].

In this investigation, the muon rate will be used to quantify seasonal differences. This rate has been demonstrated to also depend exponentially on the distance travelled. In order to simplify future analysis, the rate dependence on depth is given rather than on geometric distance. Mathematically:

$$R(d) = R_0 e^{-ad} \tag{2.10}$$

where d represents the depth of the detector. This relation is expected to be a reliable measurements of the muon rate.

[†]It is worth nothing that muons reaching a depth of 3500 meters under water will have energies of $\geq$ 1833 GeV [6] and thus will travel at speeds of v $\approx$ 0.99999999667c.

2.3 Atmospheric variables

Depending on the different variables of the atmosphere, pions and kaons may be more likely to interact or decay. Since muons are only created when decays take place, we expect an increase in the muon rate when the characteristics of the atmosphere are optimal for such an event. In this research project, the characteristic studied will be the temperature of the atmosphere.

As stated earlier, the intensity of the muon rate is given as

$$I(r) = I_0 e^{-\frac{r}{c\tau}} \tag{2.11}$$

This formula can also be expressed as as a function of the slant depth, which calculates the amount of material cosmic showers will travel through. [3]. This is given as:

$$X = \int_h^\infty \rho(h')dh' \tag{2.12}$$

where ρ represents the density of the atmosphere. This formula is only valid for vertical or almost vertical paths. This study will focus on muons with such paths.

After some mathematical manipulation we obtain

$$I(X) = I_0 \exp\left(\frac{-X\sigma N_a}{M}\right) \tag{2.13}$$

where M is the molar mass and σ is the cross section. Therefore, the amount of particles decreases with depth and increases with density [7]. If the atmosphere is assumed to behave as an ideal gas, density depends linearly on temperature through $PV = nRT$. Therefore, a change in temperature ΔT will trigger a change in muon intensity ΔI leading to:

$$\frac{\Delta I}{\langle I \rangle} = \alpha_T \frac{\Delta T}{\langle T \rangle} \tag{2.14}$$

where α_T is the temperature coefficient[†].

Since we will looking at the muon rate rather than intensity, the previous formula is translated into a rate by carrying out the following operation:

$$R = I\epsilon A_{eff}\Omega \tag{2.15}$$

[†]For a more in depth derivation and an expression for α_T please refer to [6].

Version of July 5, 2022– Created July 5, 2022 - 14:12

where ϵ is the energy of the muon, A_{eff} the detector effective area and Ω the opening angle. Finally,

$$\frac{\Delta R}{\langle R \rangle} = \alpha_T \frac{\Delta T}{\langle T \rangle} \tag{2.16}$$

Therefore, we expect a higher muon rate in the summer when temperatures are systematically higher than in the winter.

2.4 Cherenkov light

The best known constraint imposed by the universe is that of the speed of light: no object can travel faster than $3.8 \times 10^8 \text{ms}^{-1}$. However, light does not always travel at this speed. Depending on the refractive index of the medium, light may be slowed down, producing interesting optical effects such as the popular example of a pencil appearing to bend in a glass of water.

In a dielectric medium, a charged particle in motion will lead to slight electron displacements of the molecules, polarizing the medium. If this particle moves faster than the speed of light in that medium, it will create electromagnetic radiation through constructive interference and a cone of blue light will emerge. This is given the name of "Cherenkov radiation." [9].

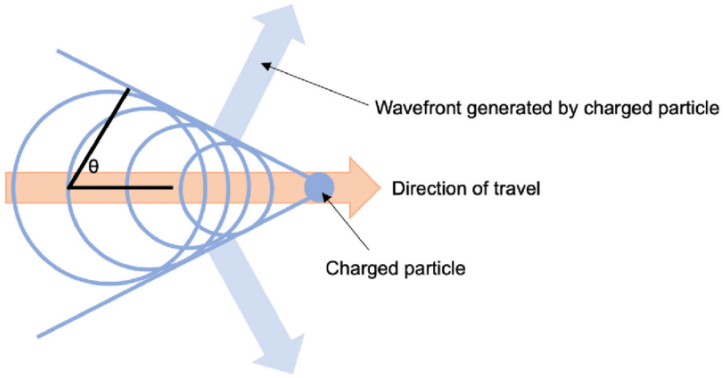

Figure 2.2: *Particle travelling in the x direction producing a wave front travelling at c, the speed of light [8].*

Therefore, when charged particles such as muons enter water at a speed faster than that of light in water, a cone of blue light is produced.

A graphical example is shown in Figure 2.2. In this diagram, muons travel along the x direction exciting the molecules around, which in turn produce photons that interfere creating a wavefront that moves at the speed of light.

Mathematically, if a medium has refractive index n and light travels at a speed v_{ln} in that medium, the minimal velocity to produce Cherenkov radiation is [10]:

$$v_{CR} = \frac{v_{ln}}{c} > \frac{1}{n} \tag{2.17}$$

Substituting $n = 1.33$ for the refractive index in water, we obtain a minimum value of

$$v_{CR} > 0.75c \tag{2.18}$$

Therefore, muons must travel at at least 0.75c. This is indeed the case as muons are not slowed down in water [11]. As it will be explained in chapter 3, KM3NeT makes use of the photons produced during Cherenkov radiation processes in order to detect particles.

2.5 Background noise

Experiments in laboratories aim to minimize the possible sources of errors and noise. However, being built in the depths of the Mediterranean sea, KM3NeT has numerous sources of background noise that will have to be considered if a reliable muon rate is to be obtained. In this section we will shortly explain how these arise.

2.5.1 ^{40}K Decay.

Potassium 40 is a radioactive isotope found abundantly in the Mediterranean sea that can decay into ^{40}Ca by β-decay or into ^{40}Ar by capturing an electron [12]. These decays will produce an electron 89.28% of time, with enough energy to generate Cherenkov radiation. This source of radiation is constant throughout time and luckily, it is straightforward to eliminate, as shown in the methods section.

2.5.2 Bioluminescence

Since no light from the sun reaches such depths in the sea, the different lifeforms that inhabit it make use of self-produced bursts of light with hopes of attracting preys, scare off predators and communicate [13]. KM3NeT detectors are triggered as a result. Therefore, when raw data reaches shore, events are filtered out depending on the amplitude and time interval in which they occurr, as these occassions are expected to be short and bright, in other words, with a high hit rate.

2.5.3 Efficiencies of the detectors

Each part of the detector has inherently different quantum efficiencies. Furthermore, due to the lively environment, the detectors may house certain lifeforms on their surface, not letting light reach them properly. Some

components may also affect the function of the detector such as the shade caused by the titanium belt and equator tape on glass.

2.6 Previous research

Previous investigations of possible correlation between seasons and muon rate have been carried out by a variety of experiments. One of the first studies was done with data from telescope AMANDA, at the south pole, which found a correlation coefficient between the relative muon rate and the relative temperature of $\alpha_T = 0.86 \pm 0.05$ [14]. Klaus Geyer followed with his doctoral thesis using data from telescope ANTARES, KM3NeT's predecessor. Even though he used several methods, he found no relation between muon rate and temperature [3].

A comparable project was carried out by the IceCube collaboration, AMANDA's succesesor. A proportional relation was found between muon rate and temperature seen in figure 2.3. The value of the temperature co-

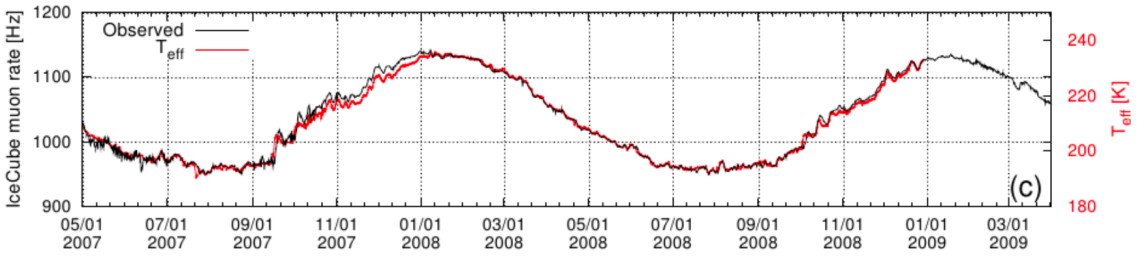

Figure 2.3: *Muon rate and temperature dependence on months at ice cube[15]*

efficient at IceCube was found to be $\alpha_T = 0.75 \pm 0.0027$ [16].

A similar study was carried out using the Opera detector, where a correlation of 0.50 and a value $\alpha_T = 0.95 \pm 0.04$ [17] were found.

Lastly, Jelmer Wagenaar completed an analogous project in his bachelor thesis with KM3NeT data. He found a correlation of 0.7 but obtained no value for α_T [7].

As shown in figure 2.4 the value of α_T is dependent on the depth of the detector.

Given the lack of a experimental value for α_T at KM3NeT and the different energy spectrums these experiments probed, this area of investigation would largely benefit from further research.

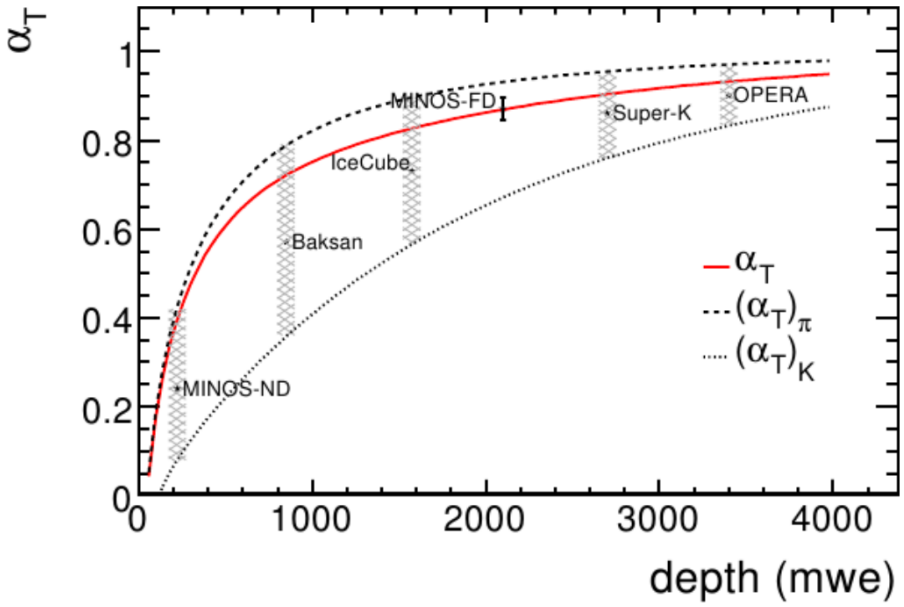

Figure 2.4: *Temperature coefficient values for different detectors depending on the depth, taken from [6].*

Chapter 3

The detector

3.1 Building Blocks

As previously discussed, KM3NeT is a neutrino telescope being built in the Mediterranean sea. Data is collected from two different sites: ARCA and ORCA. Both sites have a similar working principle. ARCA or "Astroparticle Research with Cosmics in the Abyss detector" is made up of two blocks of 115 Detection Units (DU) (often called strings) while ORCA or "Oscillation Research with Cosmics in the Abyss detector" consists of one block of 115 DUs. An artist impression is shown in figure 3.1. Individual strings will be referred to as ARCA.00XX or ORCA.00XX were XX represents the identification number of the string throughout this thesis.

Each string is composed of 18 Digital Optical Modules (DOM) connected by two cables the DOMs are mounted on. The top DOM is attached to a buoy and the bottom DOM is attached to a weight, anchored to the seabed. This disposition makes sure the strings can undergo movement originated in sea currents while remaining relatively perpendicular to the bottom of the sea, thanks to the intrinsic flexibility of the structure. Figure 3.2 shows a representation of a string and a DOM.

DOMs are pressure resistant spheres of radius 21.6 cm that house 31 Photo Multipliers each (PMT) as well as a compass that allows their specific position to be known at any point in time [18]. All PMTs are accompanied by a reflector ring in order to magnify the signals. One PMT has a diameter of 85 mm.

When an event wherein Cherenkov radiation is produced takes place, each photon triggers the PMTs. This data is then translated into a current of electrons that reaches the station at shore through a cable.

The ORCA site is being built in the sea of Toulon, France at a total

depth of 2500m with a distance between DOMs of $\approx$ 9 m and a distance between strings of $\approx$ 20 m. At the time of writing there are 10 strings in use. At shallower depths, ORCA has been designed to detect neutrinos in the low GeV energy range.

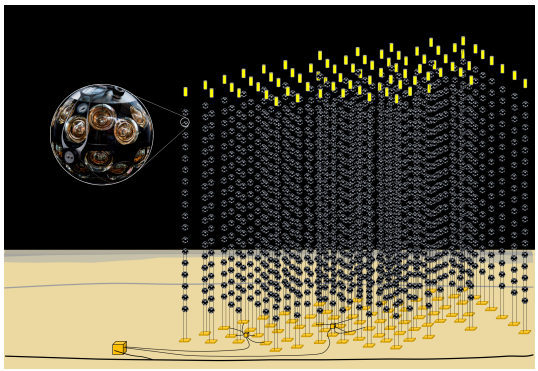

Figure 3.1: *Artist impression of the final 115 strings with 18 DOMs each [19].*

Figure 3.2: *On the left, a representation of one string. On the right, a singular DOM consisting of 31 PMTs [20].*

On the other hand, the ARCA site is being built at a depth of 3500 m, 100 kilometre away from Portopalo di Capo Passero in Sicily, Italy. With a distance of $\approx$ 90 m between DOMs and of $\approx$ 35 m between strings. At the time of writing, there are 8 available strings. Its main focus will be neutrinos with energies in the TeV range.

In this research project, focus will be directed towards ARCA due to ORCA's abundant bioluminescence activity. Specifically, ARCA6 which

consists of the 6 first strings that were deployed since some of the data that will be analyzed was recorded at a time when ARCA was composed of only 6 strings. Comparing 6 strings to 8 could lead to a further bias which should be avoided. Furthermore, ARCA.0018 stopped functiong at some point during data taking and will thus not be included in the analysis. This leaves 5 strings to evaluate.

3.2 Data Acquisition

When photons with a certain threshold voltage are produced near the detector, PMTs are triggered. The time at which this occurs as well as the amount of time the voltage stays over the threshold are sent to shore as an L_0 hit. This is accompanied by the PMT identification number. No further filtering is done at this stage. If 2 or more L_0 hits are recorded in one DOM within a time window of 25 ns, an L_1 hit is recorded. The amount of PMTs triggered by an L_1 hit is called the multiplicity.

This information is collected in so called runs. Runs are specified periods of time in which L_1 hits are continuously recorded at every PMT for all DOMs. These last several hours. The amount of total L_1 hits at every DOM for 84 runs will be investigated in this thesis.

Version of July 5, 2022– Created July 5, 2022 - 14:12

Chapter 4

Muon rate measurement

4.1 Method

In order to obtain a reliable muon rate, this exploration will make use of the depth dependence shown by atmospheric muons.

The first step will be to calculate the number of L1 coincidences at a singular DOM. This will be done by adding the coincidences from all PMTs in that DOM. Figure 4.1 shows the distribution of the coincidences as a function of the amount of PMTs triggered, also known as the multiplicity. These are the values that will be added to obtain the DOMs total counts. Every DOM in every available string will undergo this treatment. It is expected that the DOMs at the top of the strings will receive more signals than those at the bottom as shown by the KM3NeT collaboration in figure 4.2.

This is called the depth dependence. In principle, recording the amount of coincidences for a singular DOM should be enough to represent a rate and understand seasonal variations. However, by looking at the depth dependence we establish a robust method to assess whether the DOMs are behaving as expected.

The depth dependence of all strings will be plotted and the resulting curve will be fit to equation 4.1.

$$R(d) = R_0 e^{-a(d-2740)} \tag{4.1}$$

This equation is similar to that given in 2.3 but it is adapted to the depth of the detector, allowing R_0 to represent the muon rate at 2740 m below sea level. The fit parameters will be extracted for analysis. In order to notice seasonal changes, the error of the fit parameters R_0 and a should be less

than 1%. Therefore, the first half of the project will focus on making the moun rate as accurate as possible.

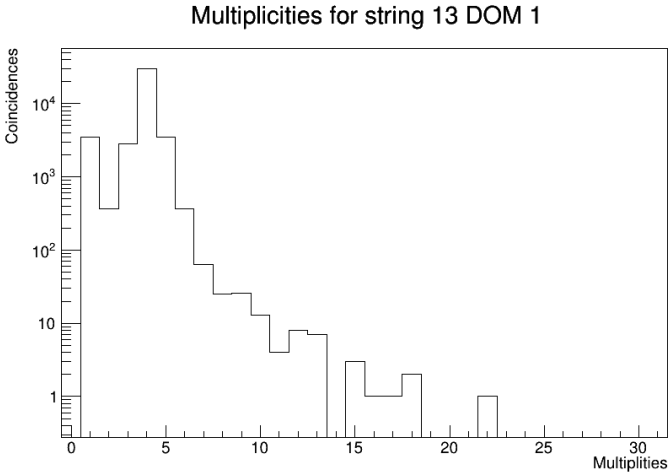

Figure 4.1: *Amount of coincidences dependence on multiplicity.Before multiplicity 8, behavior is different. This is caused by ^{40}K decay.*

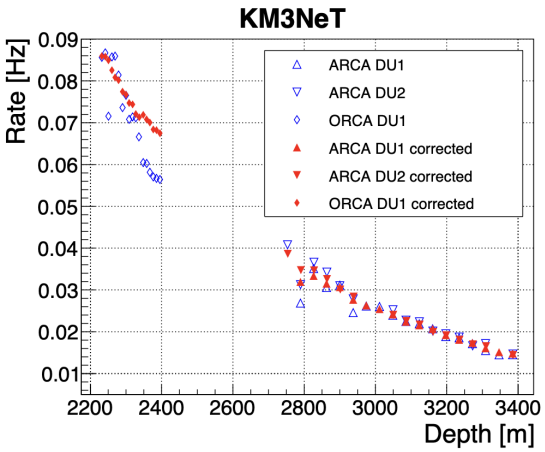

Figure 4.2: *Aim of the depth dependence graph, produced by the KM3NeT collaboration in 2020 [21].*

In the interest of accuracy, before fitting the curves there will be three corrections concerning the types of background noise explained in section 2.5. These corrections are related to the efficiencies, multiplicities and runtimes.

After, the parameters will be plotted against the days in which the runs were obtained. The slope is expected to remain constant while the muon rate R_0 should distribute according to the temperatures.

4.1.1 Efficiencies

Efficiencies are obtained by the KM3NeT collaboration through the comparison of correlated hit rates in PMT pairs within a DOM to the parametrization of the expected rate as a function of PMT distance, based on monte-carlo simulations. This is stored as efficiency information per PMT per DOM. For each DOM, we obtain the average efficiency through a number of methods which are then subject to comparison.

The first method consists of a standard average giving each PMT in a DOM the same weight, looking at muons coming from all directions.

However, we are mainly interested in those muons that fall vertically on the detector and do not deviate as that can add an undesirable bias. Therefore, a second method will make use of a weighted average, giving the top PMTs a weight of 1 and the lower PMTs a weight of 0.5 as shown by equation 4.2.

$$E_T = \sum_{i=0}^{30} w_i E_i \tag{4.2}$$

The next method is shown in equation 4.3. In this way, efficiency corrections take into account Cherenkov light that originates in radioactive decays in the DOM glass spheres. This can be useful for DOMs with greater sedimentation.

$$E_T = \frac{1}{31} \sum_{i=0}^{30} \sqrt{E_i^2 + 0.1^2} \tag{4.3}$$

The last method considered takes an average solely over the top PMTs and hence the equation becomes 4.4.

$$E_T = \frac{1}{13} \sum_{i=0}^{12} E_i \tag{4.4}$$

The aforementioned depth dependence graphs will then be normalized for the efficiencies. This will be done by dividing the coincidences by the average efficiencies of the DOMs.

These corrections will be examined by comparing how far each string is from a preliminary best fit curve. This will be quantified through the

root mean square error which is given by equation 4.5.

$$RMSE = \sqrt{\frac{\sum_{i=1}^{n} fit_i - data_i}{n}} \tag{4.5}$$

4.1.2 Multiplicities

By studying the amount of PMTs triggered by a Cherenkov event or, in other words, the multiplicity, we are able to distinguish between possible origins of the triggers. Coincidences at each DOM are thus counted after a certain number of PMTs triggered. Thorough investigation at KM3NeT has demonstrated that up until a multiplicity of 8, ^{40}K decays are dominant in the amount of coincidences. This can be clearly seen in figure 4.1 where coincidences behave different before a multiplicity 8.

The efficiency corrected depth dependence graphs will then consider several multiplicity cuts as a method to extract the cut with least information loss and smallest degree of error.

4.1.3 Runtime

It may be that certain runs are recorded over a longer or shorter period of time than others. In order to make sure that the number coincidences is comparable for all runs, the amount of hits will be divided by the length in seconds of the runtime, resulting in a rate.

4.2 Results

The investigation began with the obtention of depth dependence graphs for all strings with a multiplicity cut of $m \geq 8$ as it is considered the standard cut. These were then corrected by different methods of obtaining an average efficiency. The efectiveness of each method was gauged through a heat map distribution of the root mean square error. An example of this is shown in figure 4.3. In the interest of clarity, this figure only shows the first 14 runs.

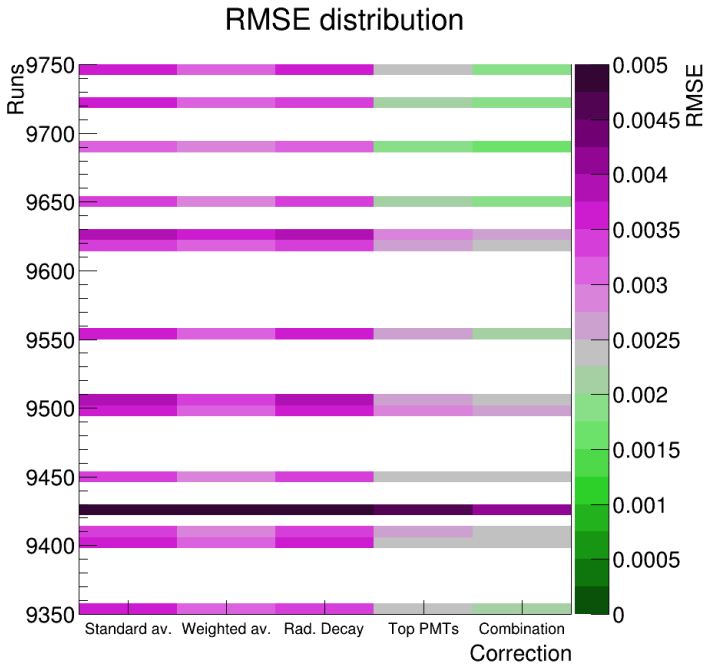

Figure 4.3: *Value of the root mean square error for each run depending on the method used to obtain an average efficiency.*

Based on the total distribution, it was decided that any run with $RMSE > 2.5 \times 10^{-3}$ should be rejected from the analysis. The preferred correction was chosen to be an average over the top PMTs for ARCA.0009 and a weighted average for the rest of the strings, this is labeled as "combination" in 4.3.

Different multiplicity cuts were the following subject of investigation. Having correct for the efficiencies, the depth dependence from 7 through 12 was plotted for run 9350 as shown by figure 4.4.

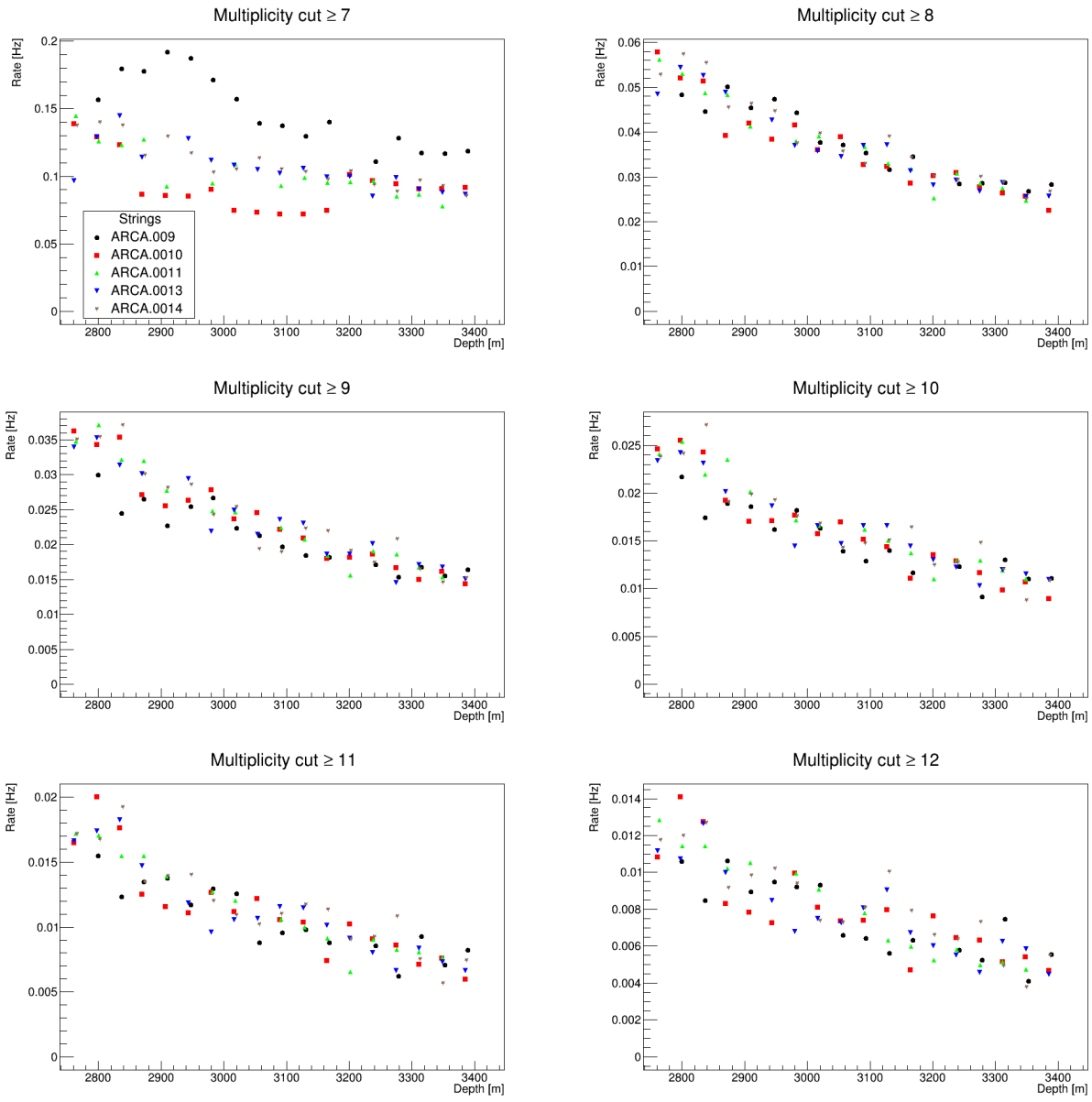

Figure 4.4: *Behavior of the different multiplicity cuts for run 9350 reflected in the rate of muons dependence on the depth of the detector. Multiplicity cut 7 shows significant scattering as opposed to the rest. This is caused by ^{40}K decay. Multiplicity cuts after 7 mostly affect the value of the intercept.*

Examining the characteristics brought out by these, it was decided that the following step should be understanding how these affect the fit parameters R_0 and a. Therefore, each data point was given the distance to the fit curve as error (root mean square) and another fit was performed. An example of the fit is shown in figure 4.5. The values for the fit parameters

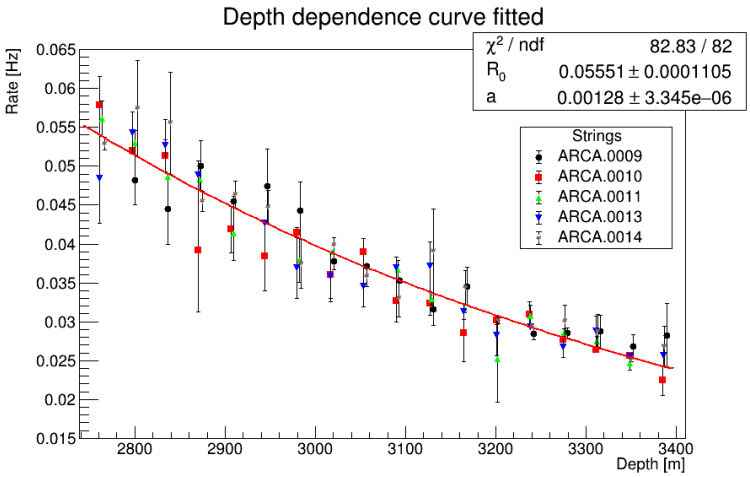

Figure 4.5: *Rate of muons dependent on depth. Data points' error is given by their deviation from the fit. Strings are plotted in different shapes and colors in order to identify them. Lower DOMs clearly receive a lesser rate of muons than top DOMs.*

and their respective errors were extracted. An example of these for run 9350 is shown in table 4.1 and the distribution for different runs is shown in figures 4.6 and 4.7. Note that in 4.7, multiplicities before 8 have been discarded.

	a $(\times 10^{-3})$	Error $(\times 10^{-6})$	%	R_0	Error $(\times 10^{-5})$	%	χ^2/dof
m $\geq$ 7	0.64	$\pm$9	1.4	0.13	$\pm$72.4	0.56	0.96
m $\geq$ 8	1.28	$\pm$3	0.23	0.055	$\pm$11	0.20	1.01
m $\geq$ 9	1.41	$\pm$3	0.21	0.036	$\pm$5.3	0.15	1.0
m $\geq$ 10	1.38	$\pm$7	0.50	0.025	$\pm$3.7	0.15	0.96
m $\geq$ 11	1.48	$\pm$6	0.40	0.018	$\pm$2.6	0.14	0.98
m $\geq$ 12	1.43	$\pm$9	0.63	0.012	$\pm$1.5	0.12	0.99

Table 4.1: *Fit parameters and their errors as well as the χ^2 value over the degrees of freedom of the fit for run 9350 at different multiplicity cuts.*

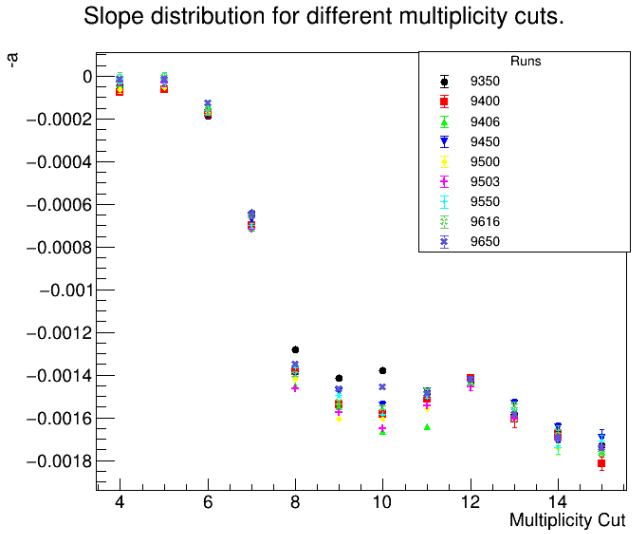

Figure 4.6: *Distribution of the slope with respect to the multiplicity cut used. No significant pattern in the behavior but it seems to remain constant from cut 8 through 12.*

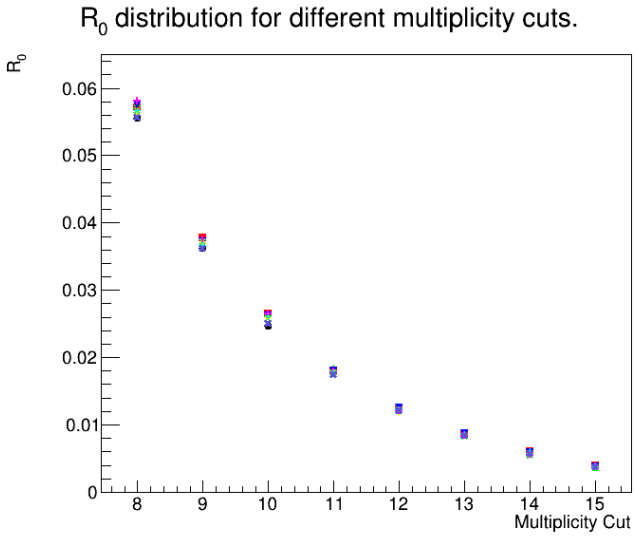

Figure 4.7: *Distribution of the normalization factor with respect to the multiplicity cut used shows an exponential decay behavior.*

It was concluded that cuts 8 and 9 would be investigated further. The distribution of the values throughout the dates in which the runs were taken has been plotted in figures 4.8, 4.9 for the normalization factor and 4.10 and 4.11 for the slope.

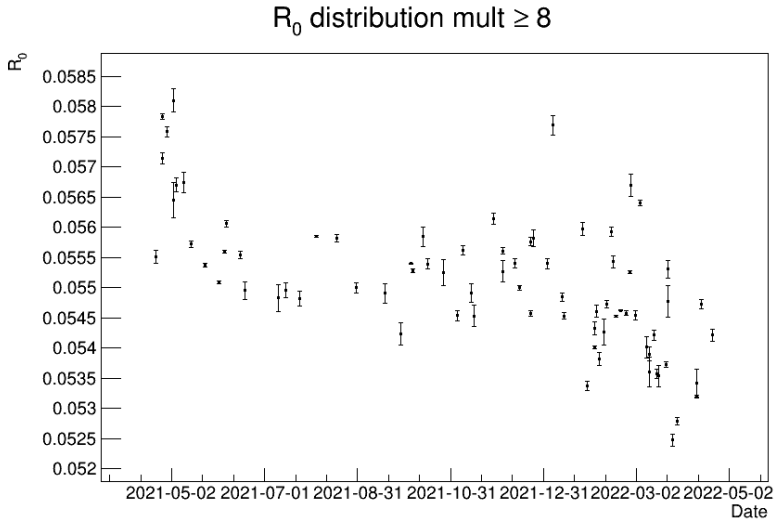

Figure 4.8: *Distribution of R_0 for $m \geq 8$ with respect to the dates in which the runs were taken.*

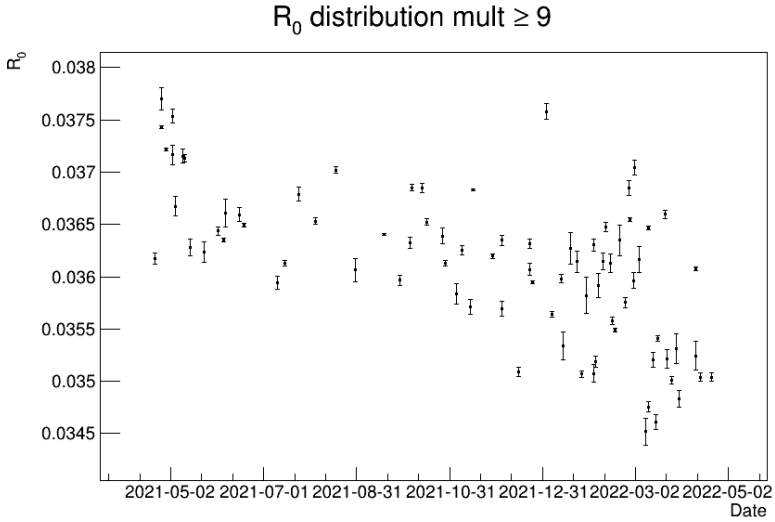

Figure 4.9: *Distribution of R_0 for $m \geq 9$ with respect to the dates in which the runs were taken.*

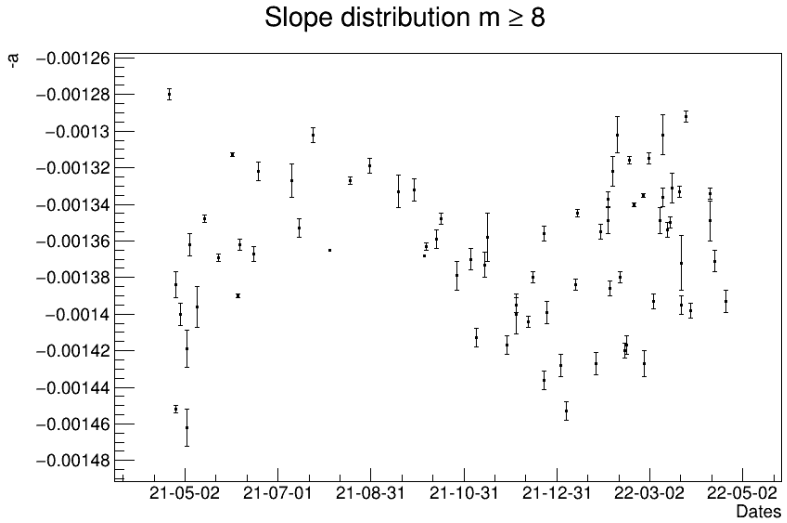

Figure 4.10: *Distribution of the slope for $m \geq 8$ with respect to the dates in which the runs were taken.*

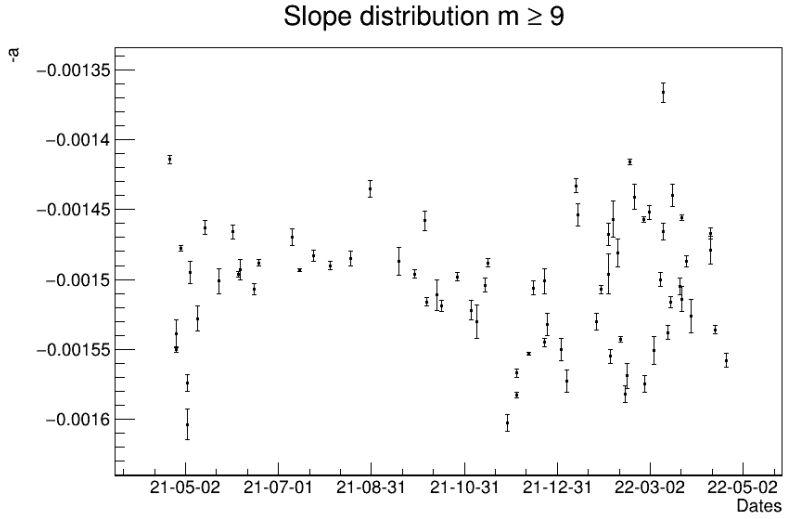

Figure 4.11: *Distribution of the slope for $m \geq 9$ with respect to the dates in which the runs were taken.*

4.3 Discussion

As stated in section 4.1 of this chapter, the goal for this division of the research project was to obtain a stable and reliable muon rate through the depth dependence relation. In order to improve the precision of the parameters, different efficiency methods and multiplicity cuts were compared.

By looking at the root mean square error for every string and obtaining an average value for each run, the separation between data points was quantified and consequently, the effectiveness of the efficiency correction was studied as shown in 4.3. Looking at the entire distribution it was found that the runs corrected through an average of the top PMTs for ARCA.0009 and a weighted average for the rest of the strings was the most effective. As presented in 4.3, this combination is the only method with a drastic decrease in the number of 'pink' runs. After further investigation, it was established that this extra correction for ARCA.0009 is needed if we want to correct for the systematically curves it presents. ARCA.0009 is the oldest string and hence the one with most sedimentation. Therefore, it is probable that there is a bias in the efficiencies. Regardless of this improvement, there were certain runs corrected by this method that presented high deviations from the preliminary fit curve. In the interest of accuracy, it was decided to reject any runs that had a RMSE value lower than 2.5×10^{-3}. Using the RMSE to discard irregular runs has proven to be a reliable method.

The next step was to look at the multiplicity cuts. From graph 4.4, it can be seen that after a cut of $m \geq 8$ the curves behave similarly. This was expected given the effects of ^{40}K on all the apriori cuts as explained in 4.1. ^{40}K decay is generally not powerful enough to light up more than 7 PMTs. This cut also seems to have the least amount of scattering. It was inferred from these graphs that the multiplicity cuts have the largest effect on the intercept values. The slope appears to behave similarly for all cuts plotted in 4.4. Therefore, the investigation continued by quantifying these observations. A fit was performed on the curves after error bars had been added as described in 4.2. This is depicted in figure 4.5. This graph shows significant yet unexpected scattering in the strings. It is possible that the efficiency corrections are not always properly estimated and hence the RMSE threshold chosen in this research project is high. In future research projects, lower rmse threshold values should be explored. The fit parameters were extracted for all runs and their distribution depending on the multiplicity cuts is shown in 4.6 and 4.7. As expected, the values from 8 through 12 for the slope are fairly constant. The behavior seems to

change after multiplicity cut 12.

With respect to R_0, the distribution appears to be an exponential decay after multiplicity cut 8. Prior cuts have been omitted as they are dominated by ^{40}K and thus behave much differently that muons, distorting the perception of the graph. Higher multiplicity cuts are related to higher energy of atmospheric muons since they have to be bright enough to light up more PMTs. Given that the higher the energy of the muons, the less likely they are to occur, it is logical that the greater the multiplicity cut the lower the rate R_0.

Table 4.1 shows an example for run 9350 of the values for the fit parameters and their respective errors as well as the accuracy of the model. The fit can be said to be representative of the experimental curves as shown by the χ^2 over the degrees of freedom value. As mentioned earlier, an error of $< 1\%$ was desired. All errors presented in the table are of the required magnitude for the intercept but not for the slope. The smallest error for both a and R_0 was found to be produced through $m \geq 9$. It was decided to study cut $m \geq 8$ as well as $m \geq 9$ since the errors are small and it allows the comparison of different energies, providing a broader context to this investigation.

Their distribution with respect to the dates can be seen in figures 4.8, 4.9, 4.10 and 4.11. The values of R_0 for cut $m \geq 8$ are much higher in May than in August. Additionally, the values in May 2021 compared to late April 2022 are much higher. It is possible that these earlier runs were not appropriately corrected for by the efficiencies, given that the root mean square error was higher than for the rest of the runs. This could create a certain bias. On the other hand, the distribution for $m \geq 9$ also had a peak in May 2021 yet the values are not drastically higher compared to August. The comparison to late April 2022 remains substantial. If the accuracy of the behavior is indeed compromised by the efficiency correction or other data issues that have not been considered, adding more runs would provide a good ground to draw conclusions. This was not possible in this project due to technical constraints.

The distribution for the slope with both cuts $m \geq 8$ and $m \geq 9$ is significantly different from what was expected. It was hypothesized that the slope would have a constant behavior in time and that the normalization factor would be the sole descriptor of the muon rate. The distribution for cut $m \geq 8$ seems to have higher values for the warmer months, with a peak in August and May. Cut $m \geq 9$ seems to flatten the distribution for a large part of 2021. This is also seen in the range of the values for $m \geq 9$ which is higher than that of $m \geq 8$, going from $\approx -.0016$ to $\approx -.00135$ as opposed to ≈ -0.00148 to ≈ -0.00126

Chapter 5

Atmospheric variations

5.1 Method

5.1.1 Atmospheric Data

Atmospheric information will be collected through NASA's AIRS3 mission [22]. This mission consists of a satellite orbiting the Earth that records the temperature of the atmosphere at every pressure level twice a day, in the mornings and evenings. An average will be obtained from those two values.

5.1.2 Correlation

After obtaining the temperature data, the slope and the normalization factor distribution will be compared to the temperature at each pressure level through Pearson's correlation which is given by formula 5.1.

$$\rho(x,T) = \frac{\sum_i (x_i - \langle x \rangle)(T_i - \langle T \rangle)}{\sqrt{\sum_i (x_i - \langle x \rangle)^2 \sum_j (T_j - \langle T \rangle)^2}} \tag{5.1}$$

Once the highest correlation is established, the distribution of the fit parameters depending on the temperature will be presented and fitted to equation 2.16 . The value obtained for the temperature coefficient α_T will allow the comparison with previous experiments not only as a check for accuracy but it will also give a value for KM3NeT's detector, adding to graph 2.4.

5.2 Results

For this section, the first step taken was the obtention of temperature data at the same coordinates as KM3NeT's ARCA site. How the temperature behaves for the different pressure levels was evaluated through a plot showing the relationship at different points in the year. This can be seen in graph 5.1. Four different dates are depicted representing the four seasons.

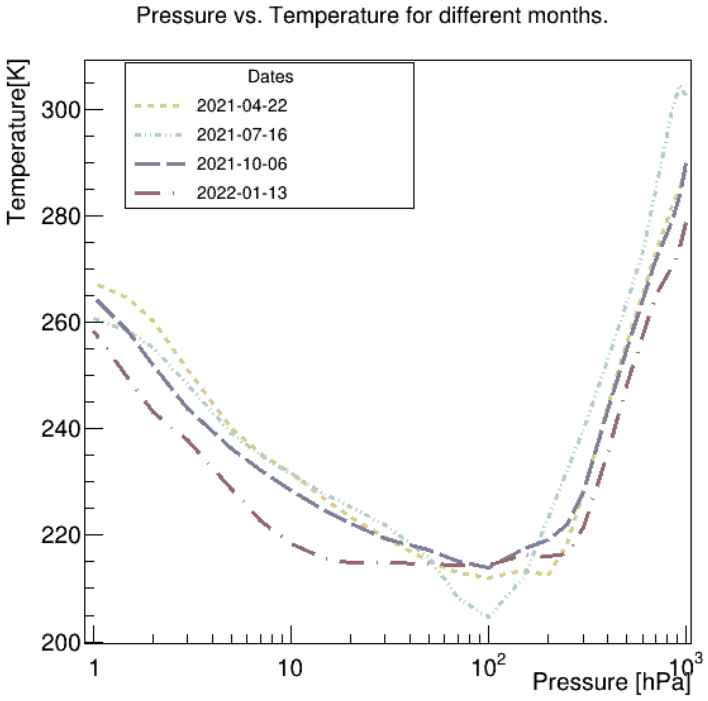

Figure 5.1: *Temperature behavior of the different pressure level throughout the months. Remains fairly constant in the upper pressure levels.*

Having considered these temperatures, a correlation between R_0 as well as the slope for both multiplicity cuts to the temperatures was calculated for every pressure level. These correlations are shown in figures 5.2, 5.3 for R_0 and 5.4, 5.5 for the slope.

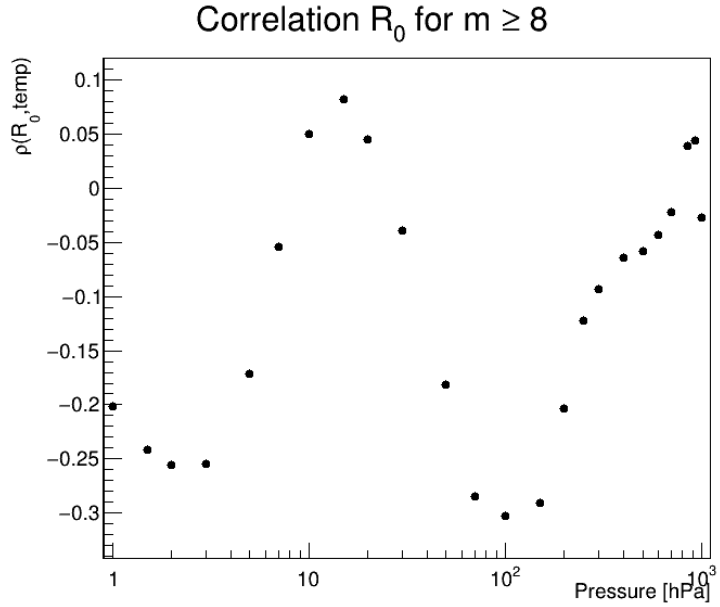

Figure 5.2: *Correlation of R_0 for $m \geq 8$ to temperature for different pressure levels. Highest correlation occurs at pressure 100 hPa of with a value of -0.30.*

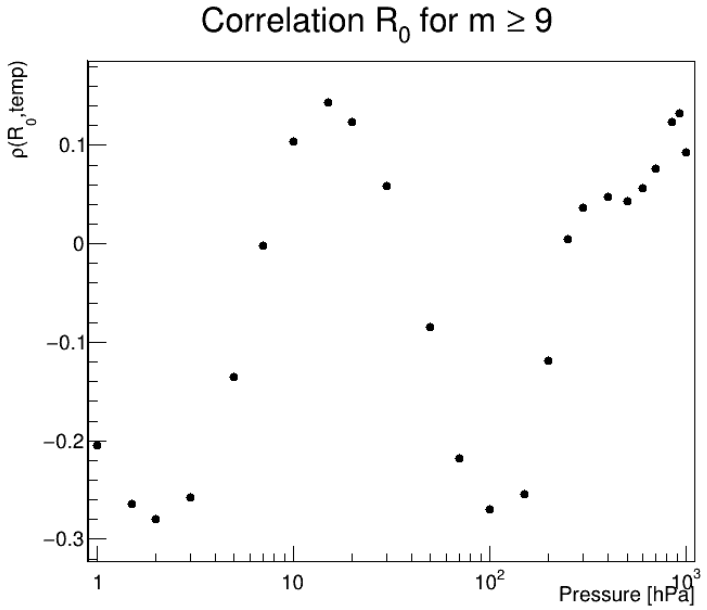

Figure 5.3: *Correlation of R_0 for $m \geq 9$ to temperature for different pressure levels. Highest correlation occurs at pressure 2 hPa of with a value of -0.28.*

Version of July 5, 2022– Created July 5, 2022 - 14:12

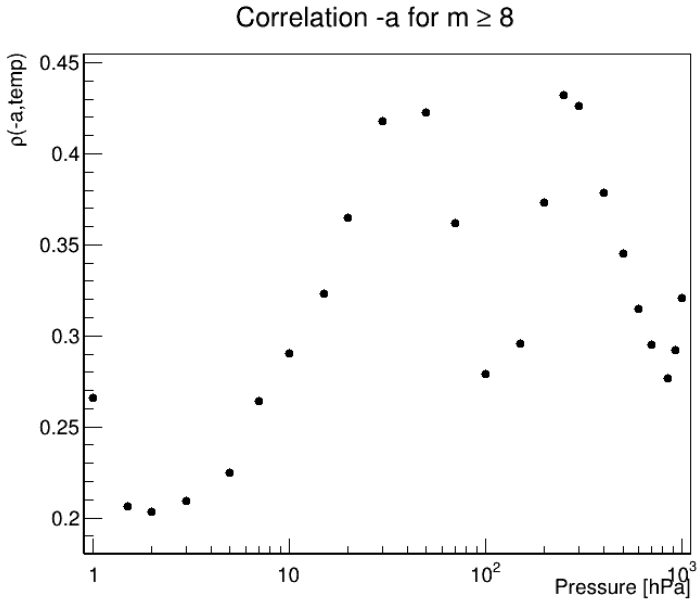

Figure 5.4: *Correlation of the slope for $m \geq 8$ to temperature for different pressure levels. Highest correlation occurs at a pressure 200 hPa of with a value of 0.43.*

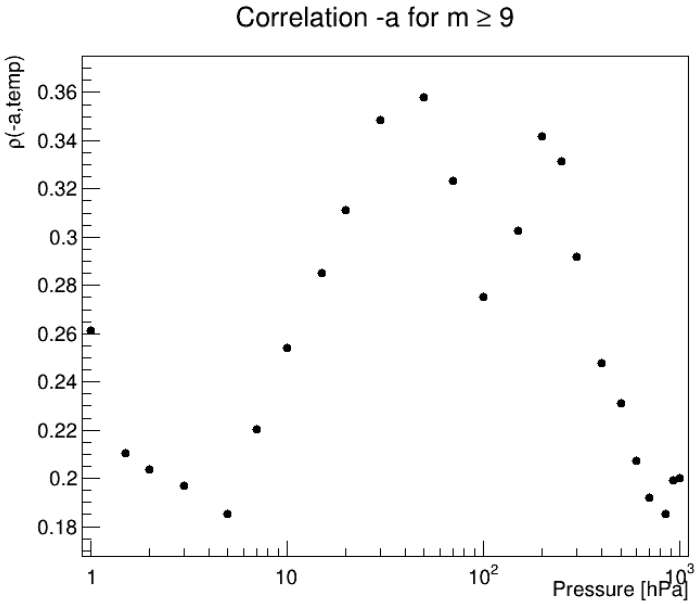

Figure 5.5: *Correlation of the slope for $m \geq 9$ to temperature for different pressure levels. Highest correlation occurs at a pressure 50 hPa of with a value of 0.36.*

These graphs were then analyzed to extract the highest correlation for each. For multiplicity cut 8, the intercept had a negative correlation of -0.30 for pressure level 100 hPa while the slope had a positive correlation of 0.43 at a pressure level of 200 hPa. On the other hand, for multiplicity cut 9, the intercept's correlation was of -0.28 at a pressure of 2 hPa and the slope's highest correlation was of 0.36 at 50 hPa.

The pressure levels with highest correlation were overlayed on top of the slope and R_0 distributions as given in graphs 5.6, 5.7 and 5.8, 5.9 respectively. The temperature data points are displayed in green triangles while the fit parameters are displayed in black circles.

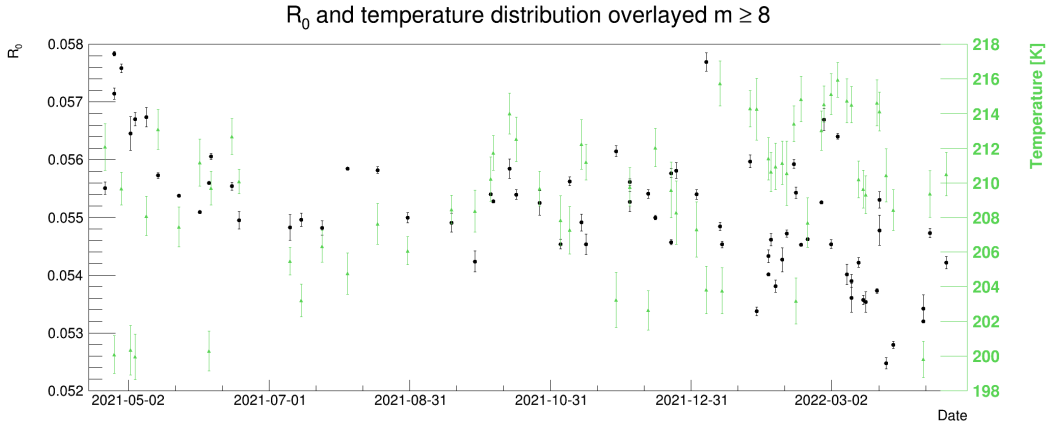

Figure 5.6: *Distribution of R_0 with $m \geq 8$ overlayed on temperature distribution at 100 hPa.*

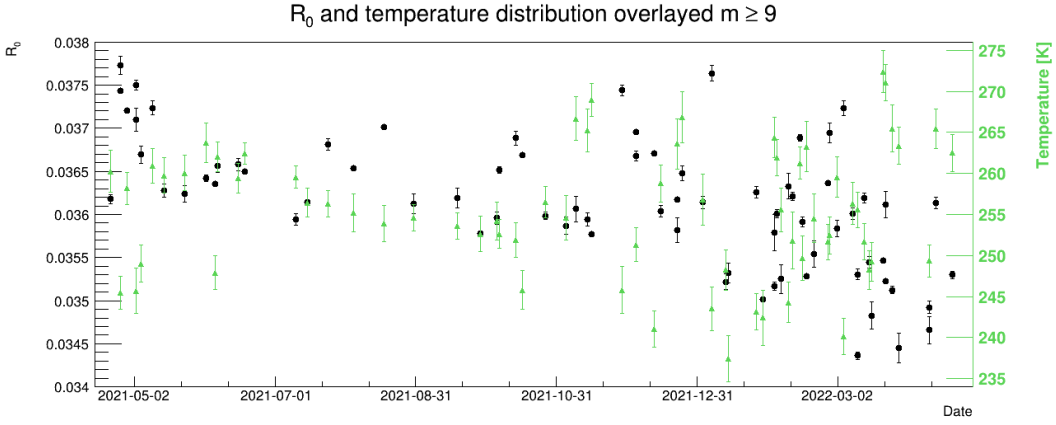

Figure 5.7: *Distribution of R_0 with $m \geq 9$ overlayed on temperature distribution at 2 hPa.*

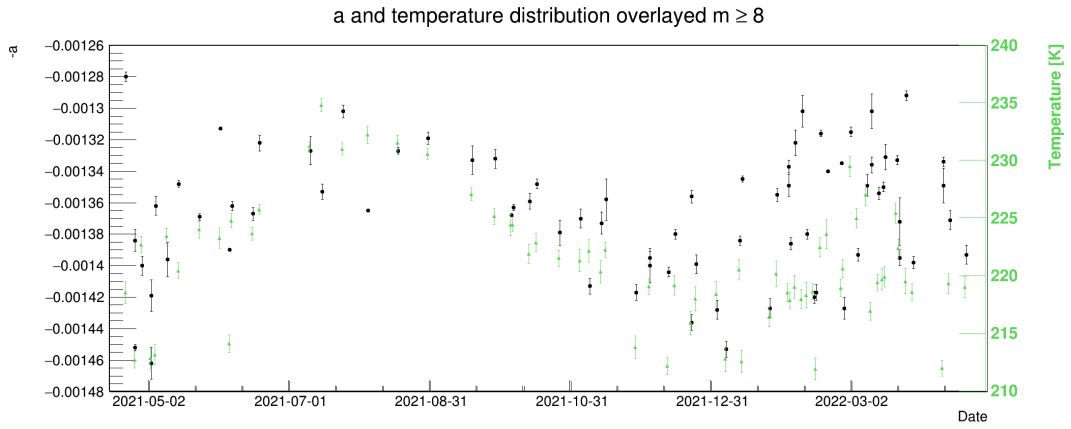

Figure 5.8: *Distribution of the slope with $m \geq 8$ overlayed on temperature distribution at 200 hPa.*

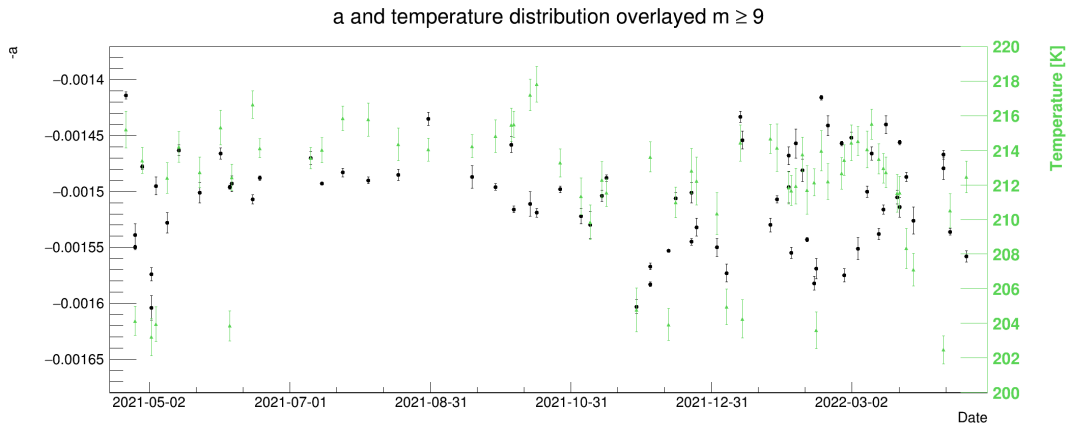

Figure 5.9: *Distribution of the slope with $m \geq 9$ overlayed on temperature distribution at 50 hPa.*

Moving forward, attention was directed towards the behavior between the fit parameters and the temperatures as shown in graphs 5.10, 5.11 for R_0 and 5.12, 5.13 for the slope. Similarly to the literature, the relation $\frac{fitpar-\langle fitpar\rangle}{\langle fitpar\rangle} = \alpha_T \frac{T-\langle T\rangle}{\langle T\rangle}$ was plotted and a value for the temperature coefficient was found for the slope as given in the graphs.

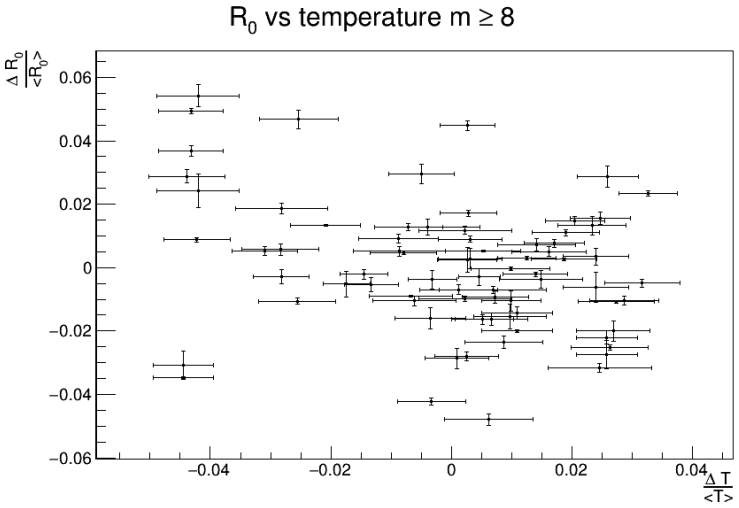

Figure 5.10: *R_0 with $m \geq 8$ against temperature showing a negative yet weak correlation.*

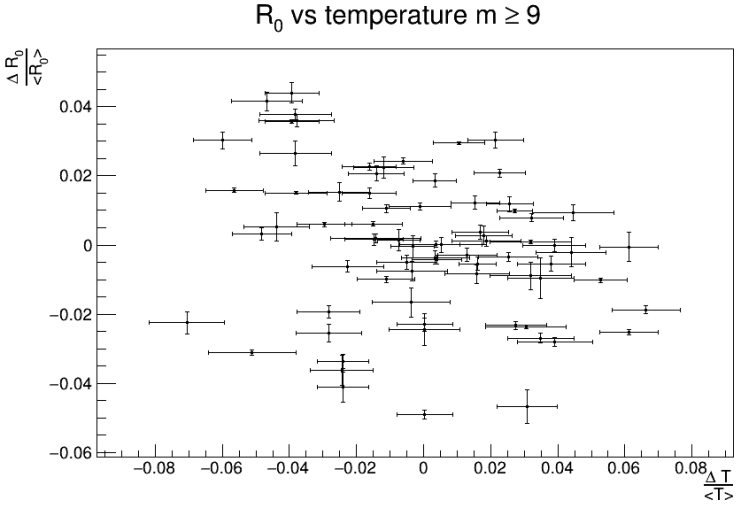

Figure 5.11: *R_0 with $m \geq 9$ against temperature showing a negative yet weak correlation.*

Version of July 5, 2022– Created July 5, 2022 - 14:12

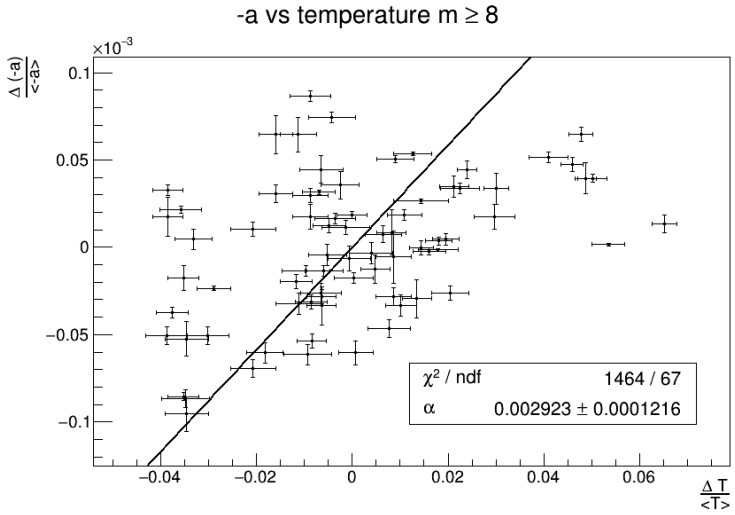

Figure 5.12: *Slope with with $m \geq 8$ against temperature showing a moderate positive correlation. Proportionality of value $\alpha_T = 0.0029 \pm 0.00012$.*

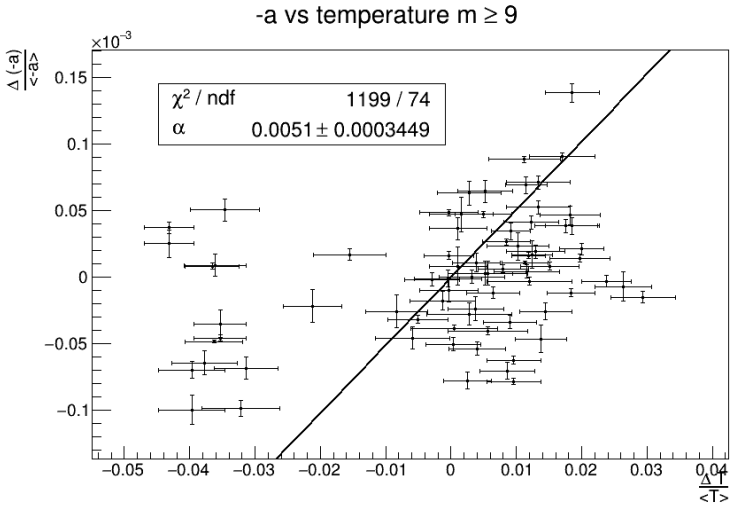

Figure 5.13: *Slope with with $m \geq 9$ against temperature showing a moderate positive correlation. Proportionality of value $\alpha_T = 0.0051 \pm 0.00034$.*

5.3 Discussion

The goal was to understand how the behavior of the fit parameters is affected by atmospheric conditions and to characterize it. In order to assess this, it is first required to understand how the atmosphere behaves throughout the different days of the year chosen. This is shown in figure 5.1.

The curves presented show a fairly constant temperature for the top layers of the atmosphere, corresponding to lower pressures. At 1 hPa, temperature ranges no more than a couple degrees Kelvin between July and January. Generally, these layers can remain at the same temperature for weeks. On the other hand, at 1000 hPa which corresponds to the surface of the Earth, the change between July and January is quite distinct, ranging from 300K to 280K.

As stated in section 2.3 and 4.1, a positive correlation for R_0 was expected at high pressure levels. However, figure 5.2 and 5.3 show the opposite. Multiplicity cut $m \geq 8$'s has its highest correlation at value -0.30 for pressure level 100 hPa. On the other hand, multiplicity cut $m \geq 9$'s highest correlation is somewhat lower, with a value of -0.28. For this cut, the highest correlation occurs at 2 hPa. This pressure is relatively low, at an altitude of only 1.5 km above sea level. The negative correlations could be explained by the behavior of the atmosphere during warmer months. Given that the atmosphere can be considered an ideal gas, the warmer the temperatures, the greater the volume. Therefore, the atmosphere becomes taller and pion or kaon decays occur at higher altitudes. This could then cause a bias in summer measurements as same energy muons will decay before reaching the detector since they will have to travel a greater distance. The muons that reach the detector are therefore more energetic. This could also explain why the highest positive correlation increases with the multiplicity cut at pressure 10 hPa. Looking at higher energy muons may decrease the bias explained. It is also possible that other variables that were not considered in this project affected the measurements, such as humidity or storms.

The overlaying of the graphs shows the weak correlation of R_0 with temperatures clearly. The data points are significantly scattered and it is difficult to see the opposite behavior between the parameters. In order to shed more light into the relationship, $\frac{fitpar-\langle fitpar\rangle}{\langle fitpar\rangle} = \alpha_T \frac{T-\langle T\rangle}{\langle T\rangle}$ was evaluated. While both graphs show a somewhat downward trend, it is clear that the behavior is not as definite and strong as expected. Therefore, no value for the temperature coefficient was found.

Version of July 5, 2022– Created July 5, 2022 - 14:12

Even though other detectors have been able to establish a high correlation at such depths, different methods were used in order to obtain a muon rate and the energies probed were not always the same range as that of KM3NeT. It would be insightful to carry out the same experiment in the ORCA site as it is built at a maximum depth of 2.5km, allowing lower energy muons to reach before decaying even during warmer months.

With respect to the slope, the values were expected to remain constant throughout the months as briefly mentioned in 4.3. Surprisingly, the slope has a moderate positive correlation with the temperature as shown by figure 5.4 and 5.5 with a value of 0.43 for cut 8 and 0.36 for cut 9.

It could be that the slope is affected by the angle of incidence and energy of the muons. Therefore, during warmer months, lower energy muons that reach the top DOMs of the detector may decay before reaching the lower DOMs. In turn, the slope would exhibit a steeper behavior and thus higher values in those months. This could explain why the correlation for cut 9 is lower than for cut 8. Higher energy muons are not as affected by the increase in the atmosphere's height.

The overlayed distributions 5.8 and 5.9 shows explicitly how the pattern for the temperature and for the slope match each other. While they do not always overlap, specially for cut 9, a trend can be concluded. This match is more remarkable in the 2021 August to December transition. For these parameters, values for the temperature coefficient were found as shown by figures 5.12 and 5.13. In the case of $m \geq 8$ this value was $\alpha_T = 0.0029 \pm 0.00012$. For $m \geq 9$, the value found was of $\alpha_T = 0.0051 \pm 0.00034$. Even though these values are relatively small and the χ^2 values quite large, they show a significant relationship between these two parameters. In future research, it would be insightful to consider these results in a broader picture, also comparing the energies and paths of the muons.

Version of July 5, 2022– Created July 5, 2022 - 14:12

Chapter 6

Conclusion

This research project has provided a new way to calculate the muon rate through the use of atmospheric muon's depth dependence. This rate was then used to compare the behavior during different atmospheric phases of the year in terms of the temperatures.

After establishing a method to obtain the depth dependence graphs, it was investigated how the efficiency corrections and multiplicity cuts affect the precision of the muon rate.

The most effective efficiency correction was obtained through the comparison of the average root mean square error of each run. We found that the best correction was a combination of two: An average over the top PMTs for ARCA.0009 and a weighted average with larger weights for the top PMTs for the rest of the strings. This slightly different correction for ARCA.0009 was necessary to correct for the systematically flat curves it exhibits. This is likely caused by a bias in the efficiency estimate due to a large amount of sedimentation considering the time ARCA has been functioning as opposed to other strings. The average root mean square error method has proven to be a successful way to check how useful the corrections are and could be of help in the future.

Depth dependence curves were then fitted to an exponential decay and the manner in which different multiplicity cuts affect these curves was studied by contrasting the values of the fit parameters and their distribution. It was found that while the slope behaves more randomly depending on the multiplicity cut, it presents similar values between cut 8 and 12. On the other hand, after multiplicity cut 8, the normalization factor R_0 behaves as an exponential decay. This agrees with the idea that the higher the multiplicity cut, the more energetic muons being considered. Muons able to light up 9 PMTs will have higher energies than those that light up 8

PMTs. It was thus decided that even though a cut of 9 provided the smallest error, it would be relevant to explore both cut 8 and 9. This would allow the comparison of energies, broadening the evaluation of seasonal variations.

Attention was then directed to changes with the seasons. It was found that R_0 for multiplicity cut 8 had a correlation to the temperature of -0.30 at a pressure level of 100 hPa while cut 9's highest correlation had value -0.28 at a pressure level of 2 hPa. These results are in opposition with the initial hypothesis as the muon rate was expected to increase with temperature. A plausible explanation could be the expansion of the atmosphere in warmer months, forcing muons to longer paths as they originate at higher altitudes. This is corroborated by the fact that at pressure level 10 hPa, both multiplicity cuts have their highest positive correlation yet the value for cut $m \geq 9$ is higher than that of cut $m \geq 8$. More energetic muons are thus less affected by a change in temperature and height of production.

Lastly, it was found that the slope has a non-constant distribution throughout the year. The value for this parameter was higher in the warmer months than in the colder ones for both cut $m \geq 8$ and $m \geq 9$. This is shown by their moderate correlation to the temperature of 0.43 at 200 hPa and 0.36 at 50 hPa respectively. Similarly to R_0, a conceivable cause for this could be the expansion of the atmosphere in the summer months. Lower energy muons that reach the top of the detector may not reach the bottom, increasing the values for the first DOMs and decreasing it for the lower DOMs making the curves steeper. Values for α were found for both cuts. In the case of $m \geq 8$ the value of alpha was found to be $\alpha = 0.0029 \pm 0.00012$ while in the case of $m \geq 9$ the value was of $\alpha = 0.0051 \pm 0.00034$.

This experiment has successfully established a new method to quantify a muon rate, taking into account all hits after potassium 40 decays. Furthermore, it has found an interesting relation between the slope and normalization factor and the temperature of the atmosphere as well as a useful way to check for the effectiveness of the efficiency corrections and the quality of the runs. However, in future research this experiment should be performed for more runs and strings, comparing several years rather than one. The threshold of the RMSE should be lowered in the interest of accuracy. Lastly, a similar project should be done for ORCA since it is less deep, possibly lowering the energy spectrum of muons reaching the detector.

Version of July 5, 2022– Created July 5, 2022 - 14:12

Bibliography

[1] Radioactivity EU, "Pauli's letter, an invisible particle to explain the missing beta energy puzzle." https://www.radioactivity.eu.com/site/pages/Pauli_Letter.htm.

[2] Cern, "Cosmic rays: particles from outer space." http://www-cs-faculty.stanford.edu/~uno/abcde.html.

[3] K. Geyer, *Measurements of the atmospheric muon rate with the ANTARES neutrino telescope*. PhD thesis, 01 2015.

[4] B. Holland, Z. Spragg, A. Kubiak, and L. Elliott, "Near-space muon flux detection and analysis," 05 2017.

[5] L. Liu and P. Solis, "The speed and lifetime of cosmic ray muons," 2007.

[6] E. Grashorn, "The atmospheric charged kaon/pion ratio using seasonal variation methods," 2010.

[7] J. Wagenaar, "Seasonal fluctuations of atmospheric muon rate," Bachelor's Thesis, 2020.

[8] M. Brookes, C. Chan, B. Baljer, S. Wimalagunaratna, T. Crowley, M. Ragbir, A. Irwin, Z. Gamie, T. Beckingsale, K. Ghosh, and K. Rankin, "Surgical advances in osteosarcoma," *Cancers*, vol. 13, p. 388, 01 2021.

[9] J. V. Jelley, "Cerenkov radiation and its applications," *British Journal of Applied Physics*, vol. 6, 1955.

[10] M. F. L'annunziata, "Radioactivity introduction and history, "cherenkov radiation"." https://doi.org/10.1016/B978-044452715-8.50010-4, 2018.

[11] B. Resnick, "Extremely powerful cosmic rays are raining down on us. no one knows where they come from," 2019.

[12] P. J. N. Braat, "Searching for neutrinos in the mediterranean sea," pp. 8–10, 2018.

[13] NASA, "What is bioluminescence?." https://oceanservice.noaa.gov/facts/biolum.html.

[14] A. Bouchta, "Seasonal variation of the muon flux seen by amanda," vol. 2, p. 108, 01 1999.

[15] S. Tilav, P. Desiati, T. Kuwabara, D. Rocco, F. Rothmaier, M. Simmons, and H. Wissing, "Atmospheric variations as observed by icecube," 2008.

[16] Icecube Collaboration, "Seasonal variations in atmospheric muon rate," 2008.

[17] OPERA Collaboration, "Measurement of the cosmic ray muon flux seasonal variation with the opera detector," 2018.

[18] H. Yepes Ramírez and B. D. Darquea Chauca, "Digital compasses calibration in km3net," 2021.

[19] KM3NeT Collaboration, "Album: Artist impressions." https://www.km3net.org/pictures-and-videos/picture-galleries/album-optical-module/.

[20] KM3NeT Collaboration, "Letter of intent for arca and orca," July 2016.

[21] KM3NeT Collaboration, "Dependence of atmospheric muon flux on seawater depth measured with the first km3net detection units: The km3net collaboration," *The European Physical Journal C*, vol. 80, 02 2020.

[22] AIRS Science Team/Joao Teixeira, "Airs/aqua l3 daily standard physical retrieval (airs- only) 1 degree x 1 degree v006 (2013)."